# Concurrent weak localization and double Schottky barrier across a grain boundary in bicrystal $SrTiO_3$

M. Egilmez,[1,2,*] S. El-Khatib,[1,2,†] F. Mustafa,[1,2] S. Ahmad,[1,2] A. Di Bernardo,[3] and J. W. A. Robinson[4]

[1]*Department of Physics, American University of Sharjah, Sharjah, PO Box 26666, United Arab Emirates*

[2]*Materials Science and Engineering Program, American University of Sharjah, Sharjah, PO Box 26666, United Arab Emirates*

[3]*Department of Physics, University of Konstanz, 78457 Konstanz, Germany*

[4]*Department of Materials Science & Metallurgy, University of Cambridge, Cambridge CB3 0FS, United Kingdom*

(Received 10 September 2022; revised 28 January 2023; accepted 14 February 2023; published 3 March 2023)

Stoichiometric $SrTiO_3$ (STO) is a wide band-gap insulator in which oxygen deficiency generates a low-temperature metallic ferromagnetic state. Here, we report weak ferromagnetic-like and metallic transport in oxygen-deficient bicrystal of STO with a low-temperature electron mobility and surface carrier density of $2800\,cm^2\,V^{-1}\,s^{-1}$ and $3.500 \times 10^{16}\,cm^{-2}$, respectively. Moreover, we show that magnetotransport behavior in the bulk and across the grain boundary (GB) in STO single crystals are significantly different. In the bulk, our magnetotransport results agree with those reported in the literature. Importantly, low-temperature magnetotransport across the GB shows a disorder-induced metal-insulator transition, and it is modeled as a quasi–two-dimensional system below 10 K that accounts for weak localization (WL), supported by electron-electron, electron-phonon, and Hikami-Larkin-Nagaoka (HLN) quantum interference models. The HLN model accounts for realistic length scales: the dephasing length $L_\phi$, and the spin-orbit (SO) scattering length $L_{SO}$, which are comparable to the electron mean-free path, resembling the surface-conducting nature across the GB. Our experimental work shows the importance of structural defects in the interpretation of magnetotransport in $SrTiO_3$ and shows that WL is concurrent with a double Schottky barrier at the GB interface.

DOI: 10.1103/PhysRevB.107.104401

## I. INTRODUCTION

$SrTiO_3$ (STO) is a promising material or substrate for oxide electronics as it has tunable electrical properties [1–6]. STO has a perovskite unit-cell structure, which in stoichiometric bulk form has an indirect band gap of 3.2 eV separating the $2p$(O) valence band and the $3d$(Ti) $t_{2g}$ conduction band [7]. Electron doping via Nb (wt 0.1%) results in metallic electron transport as well as optical transparency. Metallic-like electronic conduction in the bulk can be achieved by annealing under vacuum at high temperatures or under high-intensity UV light irradiation, which creates surface oxygen vacancies. Oxygen vacancies in STO also lead to magnetism [8–11].

Oxygen vacancies in STO are common point defects. They generate fascinating physics since their density and distribution lead to tunable magnetic and electric properties [12–14]. When oxygen is removed from STO, the formation of a neutral defect is balanced by the creation of two mobile electrons [2,8,10,15,16]. An isolated vacancy can thus be treated as a hydrogenic double donor in which the magnetic moment is present for particular electron or oxygen vacancy concentrations [3,17]. It has been shown that the arrangement of the neighboring vacancy sites as monovacancies or multivacancies, charge-carrier density, and vacancy-vacancy interactions define the magnetic interactions in STO [3,18]. Removal of the oxygen alters the hybridization of the Ti orbital via distortion of the oxygen octahedra. In the perovskite structure of STO, $O^{2-}$ anions bond to $Sr^{2+}$ cations at the cube vertex and $Ti^{4+}$ cations at the cube center. In an optimally oxygenated unit cell of STO (lattice parameter 3.94 Å), the Ti cation is sixfold coordinated with the anions forming an octahedron. The highest solid-state occupied bands contain 18 electrons primarily in oxygen $p$ orbitals hybridized with both cation orbitals. The lowest unoccupied bands are composed of Ti $3d$ $t_{2g}$ states yielding an indirect band gap. In addition, the removal of the oxygen from the structure results in strong Jahn-Teller distortion in STO where its crystal symmetry and configurational energy are reduced [3,19,20]. Lowering crystal symmetry leads to a local expansion of the volume of $\approx$1%, a tilting of the oxygen octahedra, and an increase of the Ti-Ti distance upon the formation of a new $\sigma$ bond at the vicinity of the vacant oxygen site. In this respect, the local electron correlations between the neighboring oxygen-deficient sites, and the structural rotation of the oxygen octahedron along with free charge-carrier density determine the nature of magnetism in STO. Bezanilla *et al.* extended the mono- and multivacancy description of magnetism to the charged clusters of oxygen vacancies for various geometries in which permanent magnetic moments can be observed depending on the charge-carrier density [3].

Experimentally, superconductivity [21], metal-insulator transition [9], colossal positive magnetoresistance [14], surface magnetism [17,22], blue-light emission [23], and giant photoconductivity [24,25] have been observed in reduced STO in bulk, thin film, single crystal, and two-dimensional (2D) electron gas heteroepitaxial structures with $LaAlO_3$

*megilmez@aus.edu
†selkhatib@aus.edu

 

(LAO) [26]. Moreover, oxygen stoichiometry has a significant role in the stabilization and tunability of the antiferrodistortive and ferroelectric phases in STO [27].

The above discussion demonstrates the significant role played by oxygen-related defects in determining the optical and magnetoelectrical properties of STO. Magnetotransport in STO and LAO/STO is important for oxide electronics and can be related to colossal spin-orbit coupling, Rashba spin-orbit interaction, and weak localization [28,29]. However, the general nature of defects in STO is not limited to oxygen vacancies [22,30,31]. It has been shown that Sr vacancies [30], Ti antisites in STO [32], point defects, dislocations, and grain boundaries (GBs) with broken translational symmetry can alter the couplings between spin, lattice, and charge degrees of freedom.

However, and despite the existence of extensive literature on atomic vacancy (mostly oxygen) defects, there is limited literature on other types of structural defects such as grain boundaries. Bicrystals host a single-GB between two grains with controlled crystal orientations [15,27]. Broken symmetry at a GB can generate properties that are absent in the bulk owing to a coupling between lattice, spin, and electronic degrees of freedom. More often, studies on this topic highlight anomalous electrical transport and magnetic effects near the surface or at the heteroepitaxial interface in LAO/STO structures. In this regard, studies that can distinguish the role of oxygen vacancies from other types of structural effects are much needed to understand the role of oxygen vacancies on the surface-transport properties of STO.

In this study, we used a reduced STO bicrystal with a [001] symmetric single-tilt grain boundary of 18.4° to study electrical transport properties of a controlled structural disorder. We were able to distinguish magnetotransport in the bulk of STO from across the GB interface. Our magnetic characterization on reduced STO shows magnetic coercivity at all temperatures; and noticeable coercivities were detected below 10 K, an indication of weak ferromagnetic-like behavior. The resistance versus temperature [$R(T)$] in zero magnetic field on bulk STO shows metallic behavior over the entire temperature, $T$, range investigated, $R(T)$ is dominated by electron-lattice (in high $T$) and electron-electron (in low $T$) scattering. with a magnetic field $H$ applied, magnetoresistance [$R(T, H)$, $H$ : $\pm 9$ T] of the bulk exhibits similar metallic-like behaviour, but changes from quadratic at high $T$ to a combination of weak quadratic and strong linear signals at low $T$, a behavior that was understood by the scattering of the accumulated inhomogeneities due to oxygen vacancies in reduced bulk STO. On the other hand, our comprehensive work across the GB of STO shows a metal-insulator-transition (MIT) around 10 K. In this regard, the GB in the studied bicrystal along with the large density of oxygen vacancies leads to electronic disorder, which provides the necessary condition for WL. The WL driven by the accumulating inhomogeneities across the GB is found to be concurrent with a double Schottky barrier (DSB).

## II. EXPERIMENTAL DETAILS

Bicrystals with a [001] symmetric-tilt grain boundary of 18.4° are used in this study (Surface Net GmbH). X-ray photoelectron spectroscopy (XPS) measurements on these bicrystals do not show evidence of magnetic impurities. The bicrystals are annealed in vacuum ($\sim 10^{-6}$ Torr) for 3 h at 750 °C to reduce oxygen. Electrical resistance within the bulk and across a GB are measured using a closed-cycle physical property measurement system (Cryogenics Ltd.) using a four-point method with a nanovoltmeter. Connections are made using 25-μm-diameter Al wires. Magnetic properties are measured by SQUID-VSM, Quantum Design.

## III. RESULTS AND DISCUSSION

Figure 1(a) shows a schematic illustration of the bicrystal STO with the four-probe transport measurement configuration. The location of the GB is shown as the solid line in the sketch of the bicrystal, and based on the location of the line we define our four-probe measurement configuration for the bulk [Fig. 1(a), left] and across the GB [Fig. 1(a), right]. Figure 1(b) shows an XPS scan with Sr, Ti, and O at the expected binding energies [33,34]. Note that no peaks were observed at the expected binding energies for Fe, Co, and Ni; an indication that our crystal has no magnetic contaminations within the accuracy of the measurement setup. The $R(T)$ in Fig. 1(f) shows a metallic-like ($\frac{dR}{dT} > 0$) behavior between 2 and 300 K in agreement with literature [1,34–39]. A strong drop in $R(T)$ in cooling down to around 10 K, and then the metallic-like behavior $r$ shows a weaker $T$-dependence down to 2 K, suggesting different transport mechanisms taking place at low $T$ [1,37–39]. $R(T)$ is well fitted by (i) the classical metallic Fermi-liquid model that accounts for the electron-electron scattering with a quadratic $T^2$ model in the range 2–50 K [40], and by (ii) stronger metallic $T^\alpha$ model in the 50–300 K range, accounts for lattice scattering. The whole $T$ range is well fitted to:

$$R(T) = R_0 + R_2 T^2 + R_\alpha T^\alpha, \tag{1}$$

where $R_0$ is the positive resistance as $T \to 0$ [1,41]. The last term in Eq. (1) outlines the high temperature behaviour of $R(T)$, which drops fast in cooling, suggesting a stronger $T$ term that leads to $\alpha > 2$. The power $\alpha$ has been reported broadly in the literature between 2 and 5 [1,37]. A precise routine fit to the whole $T$ range should account for the small low-$T$ fitted region ($2\,\mathrm{K} < T < 50\,\mathrm{K}$) in comparison to the high-$T$ ($50\,\mathrm{K} < T < 300\,\mathrm{K}$) region. By taking each $T$ range individually, $\alpha$ converges to 2.89, close to $\alpha \approx 3$; this value suggests lattice scattering with carriers [37,40]. Fixing $\alpha = 3$, an acceptable fit (in $H = 0$) is shown in solid (red) line in Fig. 1(f), with free converging parameters, $R_0$, $R_2$, and $R_\alpha$ to $6.89 \times 10^{-3} \pm 1.11 \times 10^{-4}\Omega$, $2.45 \times 10^{-5} \pm 2.70 \times 10^{-7}\,\Omega/\mathrm{K}^2$, and $6.91 \times 10^{-7} \pm 2.26 \times 10^{-9}\,\Omega/\mathrm{K}^3$, respectively. Sheet carrier density ($n_{2\mathrm{D}} = \frac{1}{e\frac{\Delta R_{xy}}{\Delta H_\perp}}$, where $R_{xy}$ is Hall resistance, $H_\perp$ is the perpendicular magnetic field to the current, and $e$ is the charge of the electron) and mobility [$\mu = \frac{1}{en_{2\mathrm{D}}R_{xx}}$, where $R_{xx}$ is the resistance from Fig. 1(f)] on the bulk side of the crystal were in close agreement with previous reports [34,37–39,41]. Hall data were collected in the bulk of STO with the magnetic field $H$ perpendicular to the crystal surface and the electrical current. $n_{2\mathrm{D}}(T)$ and $\mu(T)$ are shown in Figs. 1(d) and 1(e). $n_{2\mathrm{D}}$ slightly drops in cooling and plateaus below 10 K to approximately $3.5 \times 10^{16}\,\mathrm{cm}^{-2}$ ($3.5 \times 10^{17}\,\mathrm{cm}^{-3}$). Note that the reported carrier-density values and

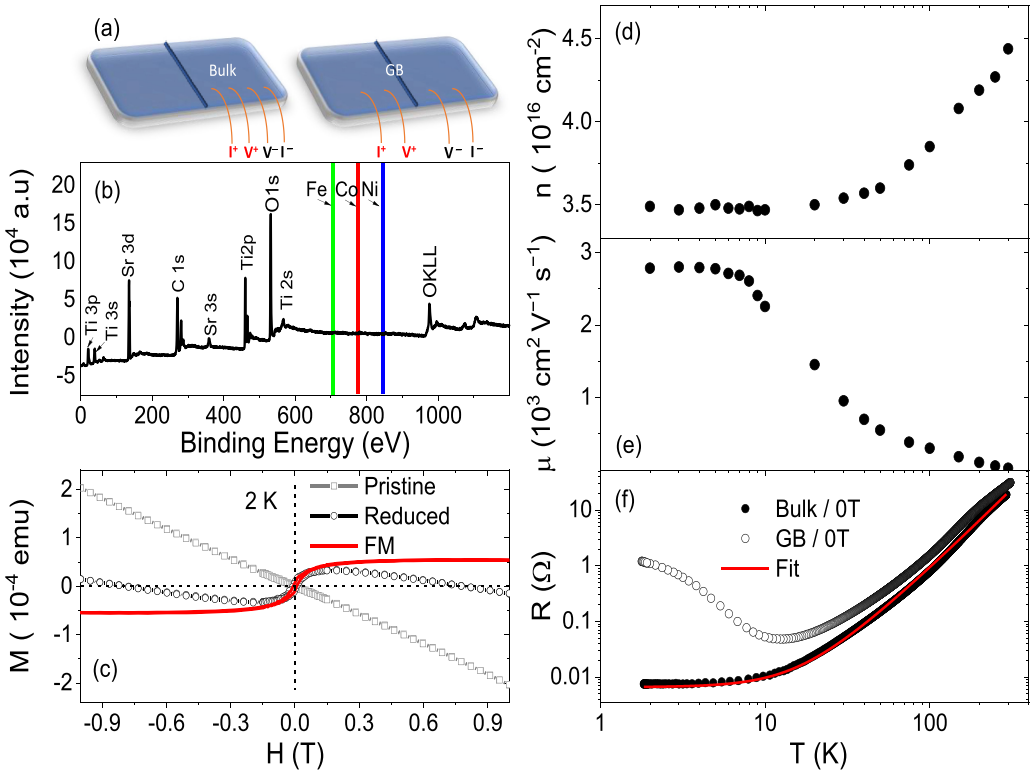


FIG. 1. Schematic diagram of the STO single crystal; the actual dimension of STO is 4.0 mm × 2.5 mm × 1.0 mm. Sketch shows two modes of transport for the four wire configurations: (left) bulk measurements with current and voltage on one side of the crystal; and (right) GB measurements across the crystal mismatch boundary with positive terminals $I^+V^+$ on one side, and negative terminals $I^-V^-$ across the GB. (b) Wide-scan XPS on one side of the bulk of STO showing Sr, Ti, and O intensities at the right positions. Green, red, and blue lines mark the positions of the Fe, Co, and Ni (which are absent). (c) Magnetic field dependence of magnetization on GB STO crystal for pristine (gray open square), reduced (black open circle), and ferromagnetic (red line). Ferromagnetic signal is after subtracting high-field negative diamagnetic susceptibility from the reduced. Temperature dependence of 2D carrier density in panel (d) and mobility in panel (e) were extracted from Hall measurement on the bulk side of STO as explained in the text. (f) Temperature dependence of the resistance of the bulk (solid circle) and the GB (open circle) in zero magnetic field. The solid red line is the fit to Eq. (1).

temperature dependence shown here are in agreement with existing literature [34,37–39,41]. On the other hand, the mobility values are almost constant below 10 K (≈2800 $cm^2\ V^{-1}\ s^{-1}$) and decrease significantly in warming as lattice vibration scattering dominates in high temperatures [38,39,42,43]. Moreover, $\mu(T)$ shows no anomalies around 105 or at 40 K, cubic to tetragonal, and ferroelectric transitions, respectively (see for example Refs. [44,45]). Moreover, transport measurements in the van der Pauw configuration were performed in the bulk STO and showed almost identical data to those in Figs. 1(d)–1(f), indicating isotropic electronic properties across the surface of bulk STO. Note that, data were collected on both sides of the crystal away from the GB line considering the bulk only, and the reported results above in Figs. 1(b), 1(d)–1(f) are reproducible for surface and transport analyses.

The behavior of $R(T)$ across the GB [Fig. 1(f), open symbol] is interesting and deserves more investigation. At 300 K, the resistance is higher than the bulk; in cooling, $R(T)$ shows a metallic-like trend (similar to the bulk) down to ∼10 K where a MIT occurs, suggesting a different type of conduction mechanism at low temperatures. At temperatures lower than the MIT, $R(T)$ continues to increase (insulating-like, $\frac{dR}{dT} < 0$), which is an indication of semiconducting-like behavior. The insulating-semiconducting upturn in the GB resistance curve below 10 K suggests carrier localization. MIT could be understood in terms of different models; Kondo effect, Efros-Shklovskii (ES) variable range-hopping (VRH) localization, Mott-VRH localization, 3D, and 2D weak localization (WL) [40,43–46]. Kondo effect is ruled out as low $T$ $R(T)$ curves could not be described by $\ln(T_0/T)$, where $T_0$ is a constant. Strong ES VRH and Mott localization in low $T$ in GB are ruled out as well since $R$(T) does not strongly change in low-$T$ region as characterized by the exponential of the form $\propto e^{(T_0/T)^m}$, where $T_0$ is a characteristic temperature, and $m$ is a unique exponent that distinguishes Mott ($m = 1/3$) from ES ($m = 1/2$) [47,48]. WL scenarios are possible and need further investigation, and as one would expect, turning on $H$ at this point provides valuable information to understand the electrical properties of the bulk and across the GB in the WL mode, as discussed below [in Figs. 2(b) and 2(c)].

A crucial point to discuss before investigating electrical transport with $H$, Fig. 1(c) shows the magnetic-field dependence of magnetization $M(H)$ at 2 K on GB for the as-received (pristine) crystal; $M(H)$ resembles typical diamagnetic behavior (in open gray square). Figure 1(c) also shows $M(H)$ after reducing STO (in open black circle) at the same $T$. The $M(H)$ signal for the reduced STO has two components: (i) a weak hysteretic ferromagnetic-like component below

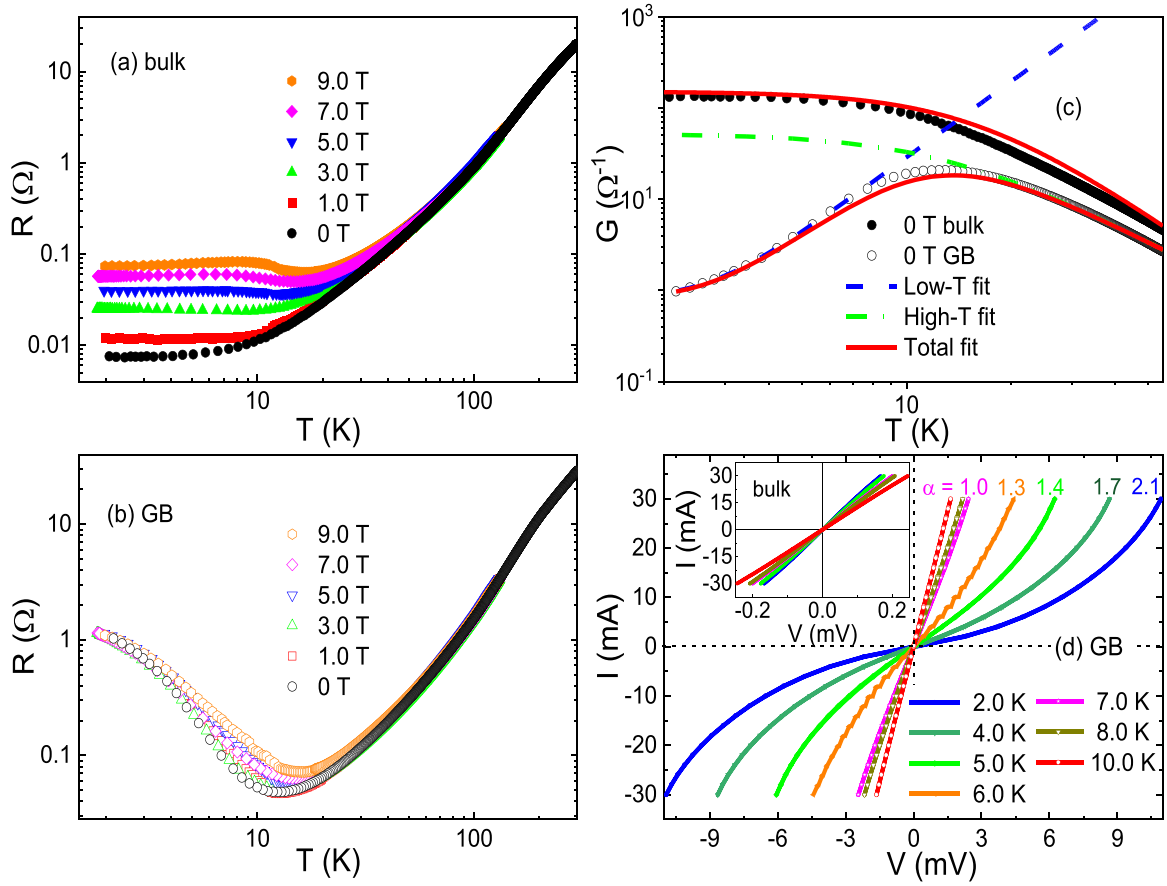


FIG. 2. Temperature dependence of resistance on (a) the bulk and on (b) the GB for STO at the displayed magnetic fields. (c) Temperature dependence of the conductance $G$ ($\alpha$ $1/R$) for bulk (solid circle) and GB (open circle) configurations. Low-$T$ and high-$T$ fits on the $G(T)$ GB curve are shown in dashed (blue) and dashed-dotted (green) lines as explained in the text. Solid (red) lines on the bulk and the GB curves are the total fits as clarified in the text. (d) The low-$T$ current-voltage curves ($I-V$) on the GB configuration, and the nonlinearities on the 2, 4, 5, and 6 K curves are scaled by the coefficient $\alpha$ as explained in the text. Inset to (d) is the $I-V$ curves on the bulk side of STO in the same temperature range of GB.

0.15 T, and (ii) a diamagnetic component at higher $H$. To look closely into the ferromagnetic signal, we separate these components as shown in the red-line data in Fig. 1(c). The weak hysteretic ferromagnetic-like component is more prominent, with coercivity of ($H_C$) $\sim$ 11 mT at 2 K. Moreover, coercivities were detected at all temperatures up to 300 K (data not shown); for example, $H_C$ at 5 and 300 K are 9 and 4 mT, respectively, in agreement with STO bulk literature [49,50]. It is worth mentioning here that reannealing the crystal in oxygen gas at 1-bar pressure diminished the magnetic behavior completely. Such observation rules out all possibilities of magnetic contamination during the annealing process. Magnetism in STO is a much-debated topic (see for example Refs. [17,49,50]). Both intrinsic and extrinsic (impurities) magnetism have been demonstrated and continue to attract much attention [3,17,21,48–52]. Oxygen vacancies in STO are broadly thought to play a vital but as yet incompletely understood role in many observed magnetic phenomena [3,17,21,50–52]. Density-functional theory calculations suggest that Ti cations neighboring the oxygen vacancies [18,53], or oxygen vacancies alone can host small localized moments in STO [54]. The wave functions of electrons between neighboring oxygen vacancies sites overlap, and crystal-symmetry changes in the perovskite octahedral structure due to the removal of the oxygen anion determine the magnetic state of the two Ti atoms on both sides of the oxygen vacancies. In other words, the magnetic state of the structure is determined by Ti-broken bonds that lead to much-localized $d$ states in the gap of the insulating host. If one considers that oxygen vacancies cluster either in the bulk or surface, the total exchange coupling of two Ti bonds facing each other across every oxygen vacancy site is strong and may lead to measurable surface magnetism [38,50]. We would like to emphasize that magnetometer measurement is a volumetric probe over the entire bicrystal and hence, the magnetism of bulk and the GB are indiscernible; for this, we investigate electrical and magnetic properties by measuring local $R(T, H)$.

Figure 2(a) shows $R(T)$ in the bulk of the bicrystal with $H$ (0 to 9 T), in the high-$T$ region (50–300 K) metallic-like $T$ dependence with relatively small magnetoresistance changes has been observed, suggesting the same conduction mechanism. At $\sim$50 K, the curves bifurcate for different $H$ showing a weaker metallic $T$ dependence and higher resistance below 10 K, however, maintaining the same overall behavior of zero-field curve up to 3 T. $R(T)$ in 0 to 3 T could be fitted with a model that was proposed above in Eq. (1). The fitting

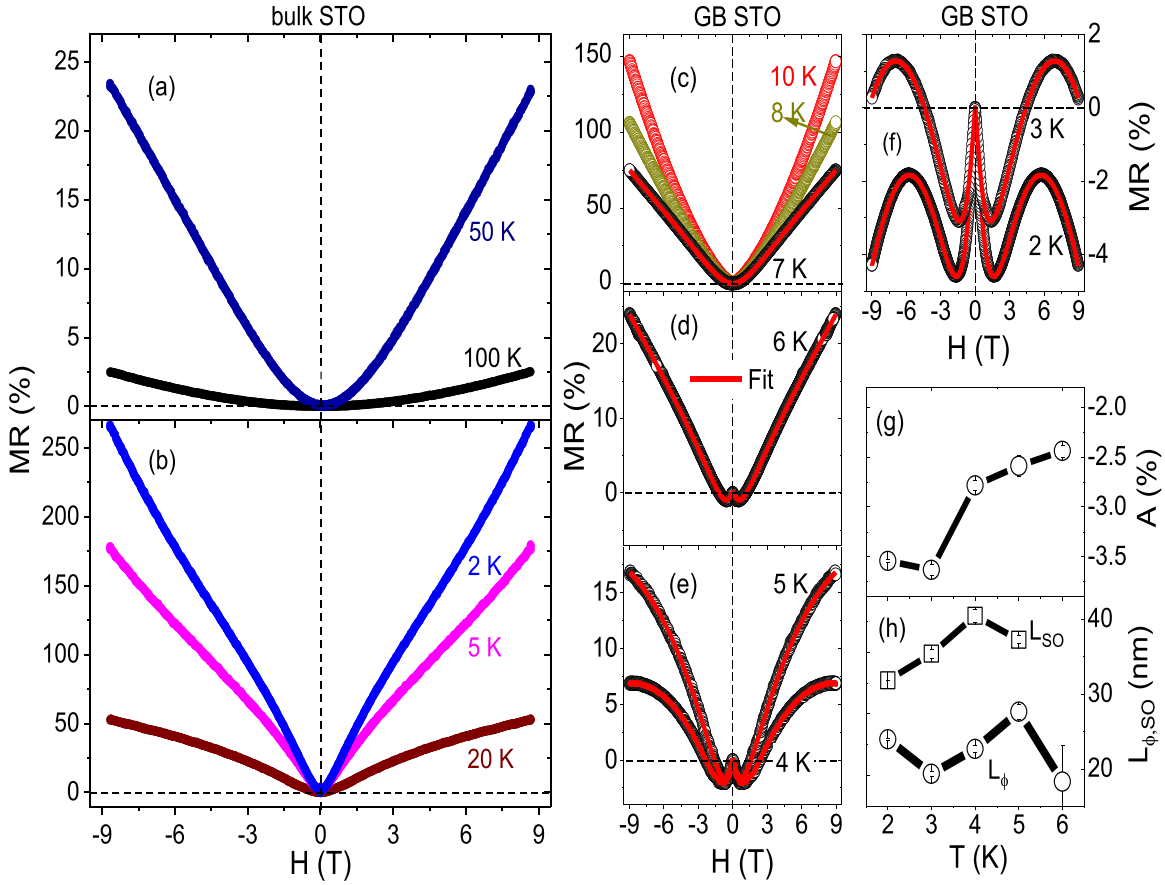


FIG. 3. Magnetoresistance MR(%) vs applied magnetic field on bulk STO in (a) 100 and 50 K, and in (b) 20, 5, and 2 K. MR (%) vs $H$ on the GB STO in (c) 10, 8, and 7 K, (d) 6 K, (e) 5 and 4 K, (f) 3 and 2 K. Solid (red) lines in (c)–(f) are the fit to Eq. (3) as described in the text. Temperature dependence of extracted parameters from Eq. (3): (g) WL term $A$, and (h) phase-coherence length ($L_\phi$) and spin-orbit length ($L_{SO}$).

is reinforced again below 50 K as shown in Fig. 2(c), where we show a zero magnetic field exemplary curve in a solid (black) circle, but now plotting the conductance $G$ ($G = \frac{1}{R}$) instead, as a function of $T$ in this low-$T$ region. The solid (red) line fits $G(T)$ very well considering the electron-electron scattering ($G\alpha 1/T^2$) model in this range as described above. Figure 2(a) shows a slight minimum anomaly in $R(T)$ curves above 5 T, followed by slightly higher resistance in cooling, and the curves again develop metallic-like behavior in cooling to 2 K. This high-field driven (>5 T) irregularity does not resemble localization effect similar to GB discussed above in Fig. 1(f), as it is followed immediately by metallic behavior in cooling down to 2 K. The origin of this minimum is attributed to competition in the mobility in the low- and the high-$T$ regions when the magnetic field is present as described by Liu *et al.* [35]. Our data show a similar trend with less pronunciation because our STO carrier density is one order of magnitude less than what Liu *et al.* have reported ($\sim 10^{18}$ cm$^{-3}$) [35].

The temperature dependence of the resistances measured in various magnetic fields [$R(T, H)$] across the GB are shown in Fig. 2(b). $R(T, H)$ shows metallic behavior in cooling from room temperature; curves coincide down to 30 K, followed by the minimum at around ∼10 K. This transition can be attributed to the thermal activation of a conduction mechanism that will be discussed further below. By applying a magnetic field, the overall behavior of $R(T, H)$ does not change significantly; however, $R(T, H)$ curves are spaced in the range 11 to 7 K and the spacing becomes less noticeable below 7 K. A close-up look into a detailed magnetoresistance analysis $R(T, H)$ below 8 K is coming in Fig. 3. In order to understand this MIT and the conduction mechanism below 10 K, low-$T$ $G(T)$ for GB in 0 T is shown in Fig. 2(c) as an example in open black circle. A metallic regime that is followed (in cooling) by an upturn on $R(T)$ is usually attributed to the 2D WL quantum interference, where the conductance shows a logarithmic temperature dependence of the form $G(T) = G_0 + \frac{pe^2}{2\hbar\pi^2}\ln(\frac{T}{T_0})$, where $G_0$ is the conductance as $T \to 0$, $p$ is the power of the quantum scattering-length factor, and $T_0$ is a constant related to the transport mean-free path [40]. However, such a 2D model failed to fit low-$T$ $G(T)$ across the GB. On the other hand, $G(T)$ below 10 K is described by three-dimensional electron-electron interaction and WL terms given by

$$G(T) = G_0 + mT^{1/2} + BT^{p/2}. \quad (2)$$

The first term is the $T \to 0$ value of $G$, the second term describes the electron-electron quantum overlapping, and the third term designates the WL corrections in this low-$T$ window [40,55]. The parameters $m$ and $B$ measure the strength of electron-electron overlapping and WL effects. $p$, on the

other hand, is the $T$ exponent of the inelastic scattering length, with $p = 1$ describing the main inelastic relaxation mechanism which is due to electron-electron collisions, while $p = 3$ resembles electron-phonon scattering [40,56]. An initial reasonable fit is obtained using Eq. (2) in 2–15 K across the GB in zero field; data pick $p$ close to ∼3, indicating dephasing limited by electron-phonon scattering. Thus, fixing $p = 3$, $G_0$, $m$, and $B$ were allowed to vary and a good description fit is shown by the dashed blue line in Fig. 2(c). The free fitting parameters $G_0$, $m$, and $B$ results are $1.342\,\Omega^{-1}$, $-0.673\,\Omega^{-1}\,\mathrm{K}^{-1/2}$, and $0.083\,\Omega^{-1}\,\mathrm{K}^{-3/2}$, respectively. At temperatures higher than the MIT across the GB, the classical *electron-electron* scattering fits the data as shown by the dashed-dotted (green) line in Fig. 2(c). The low- and the high-$T$ distinct fits cross at ∼10 K, coinciding with the experimental MIT. A total fit that describes the GB *G(T)* in the 2–50 K range is obtained by adding the two models, Eq. (2) and the $T^2$ term from Eq. (1); a satisfactory fit is shown by the solid red line in Fig. 2(c). We should mention that although Fig. 2(c) shows one example of zero magnetic field measurement, the same quality fits are obtained when the magnetic field is applied.

Electrical transport elucidates essential information across the GB by investigating the current−voltage ($I - V$) relation as shown in the main panel in Fig. 2(d), while those in the bulk are shown as an inset in Fig. 2(d). $I - V$ on the bulk are ohmic in the temperature range of 2–10 K, while $I - V$ curves show nonlinearity across the GB. In general, the current is proportional to the power of the applied voltage, which is characteristic of space-charge-limited conduction through the $I = V^{\alpha}$ relationship, where $\alpha$ is the nonlinearity coefficient, which indicates information about the conduction mechanism of the material. The strength of the nonlinearity coefficient $\alpha$ decreases as the temperature increases, from $\alpha = 2.1$ at 2 K to $\alpha = 1.3$ at 6 K; then, it becomes ohmic ($\alpha = 1$) above 6 K as the MIT is approached. The origin of nonlinearity in $I - V$ curves is accredited to the DSB, where the cationic Sr and Ti vacancies are hoarded near the GB [57–59]. DSB becomes weaker as the temperature increases ($\alpha$ decreases as temperature increases), and just before approaching MIT these vacancies are compensated by the naturally existing oxygen vacancies available in the bulk and around the GB, signaling the disappearance of the nonohmic behavior, similar to the bulk [inset in Fig. 2(d)].

Theoretical calculations, atomic structure analysis, and light-emission observations on defective STO pointed to the formation of antiferrodistortive regions, the possibilities of nonstoichiometric structure, and hence the density of the oxygen vacancies increases at the GB [27]. On the other hand, the WL is related to the naturally accumulated oxygen vacancies, which allows the stability of polaronic local moments trapped in the vacancy site as heavily discussed in the Introduction. Such polarons are coupled in the conduction band, and the strength of the coupling increases with the local lattice distortion and the presence of strain near the GB [15,26,31,32,58–62]. To summarize, the occurrence of (i) ferromagnetic-like coercivity in *M(H)*, (ii) low T WL in $R(T, H)$, and (iii) nonlinearity on $I - V$ curves, unequivocally indicate a high concentration of oxygen vacancies deep in the insulating side at $T$ lower than MIT across the GB, which also induce detectable localization, and the DSB and WL become weaker as the MIT is approached.

Measuring percentage magnetoresistance $\mathrm{MR}(\%) = \frac{R(H)-R(0)}{R(0)}100\%$, [where $R(H)$ is the resistance measured in an applied $H$, and $R(0)$ is that measured in zero field] supports these observations. MR on the bulk and across the GB are demonstrated in Fig. 3. Starting with bulk STO, MR is quadratic at 100 and at 50 K as shown in Fig. 3(a), and MR increases with decreasing temperature. This behavior is common in metallic systems, due to Lorentz's contribution of the classical orbital scattering in the perpendicular direction. The role of MR below 20 K [as $\frac{dR}{dT}$ becomes less positive in Fig. 2(a)] is somehow different as shown in Fig. 3(b), but, still increases in cooling. The quadratic nature of MR at high temperatures (in Fig. 3(a)) dispenses to a stronger linear component which increases in cooling. MR at 2 K reaches 270% at 9 T, in agreement with previous reports [14,35,63]. Linear MR is discussed broadly in many systems, including topological insulators, semimetals, and semiconductors, where the linearity role was solely attributed to the scattering of disordered inhomogeneities in these systems [51,63–67]. We believe that the linear MR in the bulk STO is governed by the carrier mobility and is driven by the high density of oxygen vacancies at low $T$; this explains the magnetic-field driven anomaly above 5 T as discussed in Fig. 2(a).

On the other hand, MR across the GB reveals a different story and it sheds more light on the observed WL nature that we have discussed earlier. Interestingly, an anomaly appears in MR in the 2–6 K range, in the same $T$ range where nonlinearity in $I - V$ is reported and ascribed to DSB. Cooling below MIT, MR at 9 T decreases from 150% at 10 K to 75% at 7 K, where the MR signal now is mixed quadratic and linear as shown in Fig. 3(c), which agrees with the previously discussed role of inhomogeneities in the bulk. Cooling below 7 K introduces a feature that is absent in the bulk STO and the high-temperature GB data. A negative MR appears in the low magnetic-field region at 6 K; then, MR becomes positive at higher $H$, and reaches 24% at 9 T as shown in Fig. 3(d). Low-$H$ negative MR at 5 and 4 K are more obvious as shown in Fig. 3(e). At higher $H$, MR becomes positive (mixed linear and quadratic-like), reaches 17% at 9 T for 5 K, and saturates above 8 T for 4 K. MR for 3 and 2 K are plotted in Fig. 3(f), and the negative dip in MR is strong. MR in Fig. 3(f) is a combination of negative signals in the 1.5–2-T range, followed by positive quadratic ones that saturate at 7 T (for 3 K) and at 5.5 T (for 2 K); MR then turns negative. Unlike the bulk STO, MR strength in GB reduces in cooling, and MR curves below 7 K are negative in the low magnetic-field region, at the same temperature range, where $I - V$ curves depicted nonlinearity.

The important nature of the GB and the region near the GB have been investigated theoretically and experimentally by introducing a few unit cells around the GB region [27], or by using a standard supercell containing 100 atoms around the lattice mismatch [68], highlighting the importance of the surface nature (few nanometers in size) of the GB in particular, and in STO in general [15,27,32,68]. Although our analyses show no direct evidence of the nature and the amount of the carrier contribution to conductivity, the carrier distribution, and the surface contribution around the GB, we believe that our MR findings on the GB are due to these nanometer-size

interfaces. This topic has been discussed widely and it reflects the strong nature of surface carriers scattering of the inhomogeneities due to the large levels of oxygen vacancies (see for example Refs. [27,32,35,68–70]). In this essence, MR data were modeled by a quasi–two-dimensional system that accounts for WL versus weak antilocalization (WAL) described by HLN quantum-interference model [71]. The differences between WL and WAL are mainly accounted for by the behavior of MR, and the prefactor constant on the HLN model. Based on the above MR description with $H$, MR due to WL is given by [71,72]

$$\begin{aligned}\mathrm{MR}(\%) = A\Bigg[&\psi\left(\frac{1}{2}+\frac{H_\phi}{H}\right)-\ln\left(\frac{H_\phi}{H}\right)\\&-2\psi\left(\frac{1}{2}+\frac{H_\phi+H_{\mathrm{SO}}}{H}\right)+2\ln\left(\frac{H_\phi+H_{\mathrm{SO}}}{H}\right)\\&-\psi\left(\frac{1}{2}+\frac{H_\phi+2H_{\mathrm{SO}}}{H}\right)+\ln\left(\frac{H_\phi+2H_{\mathrm{SO}}}{H}\right)\Bigg]\\&+BH^2+CH,\end{aligned}\tag{3}$$

where $A$, $B$, and $C$ are fitting parameters that account for the low magnetic-field WL/WAL region captured by the HLN term, the parabolic term which involves the classical cyclotronic magnetoresistance contribution, and the linear MR discussed in the bulk, respectively. $\psi$ is the digamma function, $H_{\phi,\mathrm{SO}} = \frac{\hbar}{4eL^2_{\phi,\mathrm{SO}}}$, are the characteristic field associated with different respective length scales; the dephasing length $L_\phi$, and the spin-orbit scattering length $L_{\mathrm{SO}}$, and $\hbar$ is the reduced Planck's constant. Equation (3) takes into account SO interaction, thus accounting for the WAL effects possible in materials with delicate SO coupling, as reported for STO [2,28,69,70]. Although MR shows no obvious WAL signal (positive MR in low $H$), but still capture SO coupling lengths below 6 K as we discuss below [73].

Equation (3) offers a good description of MR below 7 K as shown by the solid red-line fits in Figs. 3(c)–3(f). At 7 K in Fig. 3(c), the WL term is negligible, and MR could be fitted with linear and quadratic terms.

In Figs. 3(d)–3(f), MR curves are negative in low $H$; hence, the WL term in Eq. (3) fits this part very well. WL is strong at 3 and 2 K, followed by upturn curvature before reaching saturation; then, it curves down in high $H$. This curvature down in MR behavior at 3 and 2 K is most likely due to dominating localized magnetic inhomogeneities in high magnetic fields overtaking thermal fluctuations at low $T$. Figures 3(g) and 3(h) show the temperature dependence of parametrization term $A$ from Eq. (3), and $L_{\phi,\mathrm{SO}}$. $A(T)$ is negligible above 6 K, and increases in cooling. $L_\phi$ plateau around 25 nm, and it lacks a power-law feature for two reasons: (i) the small-$T$ window (2–6 K) where WL occurs, and (ii) most likely by the immediate strong positive MR as MIT is approached. More importantly, despite the absence of WAL feature in MR, $L_{\mathrm{SO}}$ is extracted as expected (see for example Ref. [73]), higher than $L_\phi$ in this $T$ range, and slightly decaying in cooling, highlighting the increase strength of the SO coupling in the WL regime as superconductivity is approached below 1 K in STO [74,75]. One would conjecture the WAL signal to develop in cooling below 2 K (beyond the $T$ range of this study) before reaching superconductivity $T_c$; herein, $L_{\mathrm{SO}}$ will cross $L_\phi$ at low $T$ and WL/WAL quantum scattering overshadows at $T_c$, similar to those discussed by Bhattacharyya *et al.* and Lo *et al.* [76,77]. The extracted $L_{\phi,\mathrm{SO}}$ are reinforced as if they are compared with the extracted mean-free path ($L_e$) from the Drude model. A crude calculation using $\mu = \frac{e\tau}{m^*}$, where $\tau$ is the scattering time, $e$ is the fundamental charge, and $m^*$ is the effective mass [78], and from Einstein relation $\frac{L_e^2}{\mu\tau} = \frac{k_BT}{e}$, the mean-free path is given by $L_e = \sqrt{\frac{k_BTm^*\mu^2}{e^2}}$. In low-$T$ limit, and by using our bulk mobility from Fig. 1(e) in the 2–6 K range, mean-free path averaged to $L_e \sim 25$ nm, in close proximity to $L_\phi$ but lower than $L_{\mathrm{SO}}$. Dephasing length and mean-free path of 25 nm is certainly larger than the few unit-cell size region around the GB [15,27,32,68]. The extracted nanosize length scales from the quasi–two-dimensional fits emphasize the surface nature of the region around the GB that contribute mainly to the WL.

## IV. SUMMARY

We report a magnetotransport study on a reduced bicrystal of $SrTiO_3$ with a single 18.4° tilt along [001] symmetric grain boundary as a function of $T$ and $H$. Magnetization measurements on STO show signatures of weak ferromagnetic-like behaviour with small coercivities in 2–300 K range. On the bulk STO, $R(T)$ in zero field shows metallic behavior in 2–300 K, and is dominated by electron-lattice scattering in 50–300 K, followed by electron-electron scattering in 2–50 K. Mobility and carrier density are temperature independent below 10 K and have values of 2800 $\mathrm{cm^2\ V^{-1}\ s^{-1}}$ and $3.5 \times 10^{16}\ \mathrm{cm^{-2}}$, respectively. Turning the magnetic field on the bulk, $R(T, H)$ exhibits similar metallicity as $R(T, 0)$ in cooling from room temperature, then increases in cooling below 20 K as $H$ increases, as shown in Figs. 2(a), 3(a), and 3(b). In this range, MR changes from quadratic to a weak quadratic and strong linear signal, a behavior that was understood by the scattering of the accumulated inhomogeneities due to oxygen vacancy in reduced STO. Across the GB, $R(T, H)$ data are modeled by electron-electron and WL quantum scattering in low $T$. This is supported by MR analysis, where MR is best described by a modified WL HLN model in low $T$ that accounts for the quasi–two-dimensional system. The extracted length scales reflect the surface nature of conduction around the GB. Surprisingly, the existence of the DSB, which is accredited to the negative cationic vacancies (Sr and Ti), is suppressed by the compensation from the oxygen vacancies when approaching the MIT. WL, on the insulating side, could be understood by the accumulation of the oxygen vacancies near GB, which allows the stability of polaronic localization in the vacancies sites. Such polarons are coupled in the conduction band, where the strength of the coupling increases with the local lattice distortion and the presence of strain near the GB. The current work revealed the prominence of the structural defects in observed magnetotransport data as we were able to distinguish the transport properties between the bulk of the crystal and across a single grain boundary.

## ACKNOWLEDGMENTS

M.E. and S.E.-K. acknowledge support from the American University of Sharjah through faculty research Grants No. FRG21-M-S34, No. FRG20-M-S138, and No. FRG22-E-S93. J.W.A.R. acknowledges support from EPSRC (Grant No. EP/P026311/1).



[1] X. Lin, B. Fauqué, and K. Behnia, Scalable $T^2$ resistivity in a 4 small single-component Fermi surface, Science **349**, 945 (2015).

[2] M. Jin, D. Um, K. Ohnishi, S. Komori, N. Stelmashenko, D. Choe, J. Yoo, and J. W. A. Robinson, Pure spin currents driven by colossal spin – orbit coupling on two-dimensional surface conducting $SrTiO_3$, Nano Lett. **21**, 6511 (2021).

[3] A. Lopez-Bezanilla, P. Ganesh, and P. B. Littlewood, Research update: Plentiful magnetic moments in oxygen deficient $SrTiO_3$, APL Mater. **3**, 100701 (2015).

[4] L. Li, C. Richter, J. Mannhart, and R. C. Ashoori, Coexistence of magnetic order and two-dimensional superconductivity at $LaAlO_3/SrTiO_3$ interfaces, Nat. Phys. **7**, 762 (2011).

[5] M. Egilmez, J. W. A. Robinson, J. L. Macmanus-Driscoll, L. Chen, H. Wang, and M. G. Blamire, Supercurrents in half-metallic ferromagnetic $La_{0.7}Ca_{0.3}MnO_3$, Europhys. Lett. **106**, 1 (2014).

[6] M. Egilmez, M. M. Saber, I. Fan, K. H. Chow, and J. Jung, Correlation of structural phase transition and electrical transport properties of manganite films on $SrTiO_3$, Phys. Rev. B **78**, 172405 (2008).

[7] N. Shanthi and D. D. Sarma, Electronic structure of electron doped $SrTiO_3$: $SrTiO_{3-\delta}$ and $Sr_{1-x}La_xTiO_3$, Phys. Rev. B **57**, 2153 (1998).

[8] A. Kalabukhov, R. Gunnarsson, J. Börjesson, E. Olsson, T. Claeson, and D. Winkler, Effect of oxygen vacancies in the $SrTiO_3$ substrate on the electrical properties of the $LaAlO_3/SrTiO_3$ interface, Phys. Rev. B **75**, 121404(R) (2007).

[9] K. Gopinadhan, A. Annadi, Y. L. Zhao, X. H. Huang, Z. Q. Liu, D. P. Leusink, X. Wang, and W. M. Lu, Metal-Insulator Transition in $SrTiO_{3-x}$ Thin Films Induced by Frozen-Out Carriers, Phys. Rev. Lett. **107**, 146802 (2011).

[10] C. Lin and A. A. Demkov, Electron Correlation in Oxygen Vacancy in $SrTiO_3$, Phys. Rev. Lett **111**, 217601 (2013).

[11] A. Sarantopoulos, E. Ferreiro-Vila, V. Pardo, C. Magén, M. H. Aguirre, and F. Rivadulla, Electronic Degeneracy and Intrinsic Magnetic Properties of Epitaxial Nb:$SrTiO_3$ Thin Films Controlled by Defects, Phys. Rev. Lett. **115**, 166801 (2015).

[12] F. Schoofs, M. A. Carpenter, M. E. Vickers, M. Egilmez, T. Fix, J. E. Kleibeuker, J. L. MacManus-Driscoll, and M. G. Blamire, Carrier density modulation by structural distortions at modified $LaAlO_3/SrTiO_3$ interfaces, J. Phys.: Condens. Matter **25**, 175005 (2013).

[13] X. D. Zhu, Y. Y. Fei, H. B. Lu, and G. Z. Yang, Role of step edges in oxygen vacancy transport into $SrTiO_3$(001), Appl. Phys. Lett. **87**, 51903 (2005).

[14] A. David, Y. Tian, P. Yang, X. Gao, W. Lin, A. B. Shah, J. Zuo, W. Prellier, and T. Wu, Colossal positive magnetoresistance in surface- passivated oxygen-deficient strontium titanite, Sci. Rep. **5**, 10255 (2015).

[15] S.-Y. Choi, S.-D. Kim, M. Choi, H.-S. Lee, J. Ryu, N. Shibata, T. Mizoguchi, E. Tochigi, T. Yamamoto, and S.-J. L. Kang, Assessment of strain-generated oxygen vacancies using $SrTiO_3$ bicrystals, Nano Lett. **15**, 4129 (2015).

[16] Z. Hou and K. T. Erakura, Defect states induced by oxygen vacancies in cubic $SrTiO_3$: First-principles calculations, J. Phys. Soc. Jpn. **79**, 114704 (2010).

[17] J. M. D. Coey, M. Venkatesan, and P. Stamenov, Surface magnetism of strontium titanate, J. Phys.: Condens. Matter **28**, 485001 (2016).

[18] M. Altmeyer, H. O. Jeschke, O. Hijano-Cubelos, C. Martins, F. Lechermann, K. Koepernik, A. F. Santander-Syro, M. J. Rozenberg, R. Valentí, and M. Gabay, Magnetism, Spin Texture, and In-Gap States: Atomic Specialization at the Surface of Oxygen-Deficient $SrTiO_3$, Phys. Rev. Lett **116**, 157203 (2016).

[19] O. O. Brovko and E. Tosatti, Controlling the magnetism of oxygen surface vacancies in $SrTiO_3$ through charging, Phys. Rev. Mater. **1**, 044405 (2017).

[20] R. Evarestov, E. Blokhin, D. Gryaznov, E. A. Kotomin, R. Merkle, and J. Maier, Jahn-Teller effect in the phonon properties of defective $SrTiO_3$ from first principles, Phys. Rev. B **85**, 174303 (2012).

[21] M. N. Gastiasoro, J. Ruhman, and R. M. Fernandes, Superconductivity in dilute $SrTiO_3$: A review, Ann. Phys. (NY) **417**, 168107 (2020).

[22] P. Moetakef, J. R. Williams, D. G. Ouellette, A. P. Kajdos, D. Goldhaber-Gordon, S. J. Allen, and S. Stemmer, Carrier-Controlled Ferromagnetism in $SrTiO_3$, Phys. Rev. X **2**, 021014 (2012).

[23] Y. Yamada and Y. Kanematsu, Blue light emission from strongly photoexcited and electron-doped $SrTiO_3$, J. Appl. Phys. **109**, 102410 (2011).

[24] A. Tebano, E. Fabbri, D. Pergolesi, G. Balestrino, and E. Traversa, Room-temperature giant persistent photoconductivity in $SrTiO_3/LaAlO_3$ heterostructures, ACS Nano **6**, 1278 (2012).

[25] H. Katsu, H. Tanaka, and T. Kawai, Anomalous photoconductivity in $SrTiO_3$, Jpn. J. Appl. Phys **39**, 2657 (2000).

[26] F. Schoofs, M. Egilmez, T. Fix, J. L. MacManus-Driscoll, and M. G. Blamire, Impact of structural transitions on electron transport at $LaAlO_3/SrTiO_3$ Heterointerfaces, Appl. Phys. Lett. **100**, 081601 (2012).

[27] B. Han, R. Zhu, X. Li, M. Wu, R. Ishikawa, B. Feng, X. Bai, Y. Ikuhara, and P. Gao, Two-Dimensional Room-Temperature Giant Antiferrodistortive $SrTiO_3$ at a Grain Boundary, Phys. Rev. Lett. **126**, 225702 (2021).

[28] A. D. Caviglia, M. Gabay, S. Gariglio, N. Reyren, C. Cancellieri, and J.-M. Triscone, Tunable Rashba Spin-Orbit Interaction at Oxide Interfaces, Phys. Rev. Lett. **104**, 126803 (2010).

[29] Z. Zhong, A. Tóth, and K. Held, Theory of spin-orbit coupling at $LaAlO_3/SrTiO_3$ interfaces and $SrTiO_3$ surfaces, Phys. Rev. B **87**, 161102(R) (2013).

[30] K. Tae Kang, H. Il Seo, O. Kwon, K. Lee, J.-S. Bae, M.-W. Chu, S. C. Chae, Y. Kim, and W. S. Choi, Ferroelectricity in $SrTiO_3$ epitaxial thin films via Sr-vacancy-induced tetragonality, Appl. Surf. Sci. **499**, 143930 (2020).

[31] C. Lin and A. A. Demkov, Consequences of Oxygen-Vacancy Correlations at the $SrTiO_3$ Interface, Phys. Rev. Lett. **113**, 157602 (2014).

[32] M. Choi, F. Oba, and I. Tanaka, Role of Ti Antisitelike Defects in $SrTiO_3$, Phys. Rev. Lett. **103**, 185502 (2009).

[33] G. Xing, L. Zhao, T. Sun, Y. Su, and X. Wang, Hydrothermal derived nitrogen doped $SrTiO_3$ for efficient visible light driven photocatalytic reduction of chromium (VI), Springerplus **5**, 1132 (2016).

[34] J. D. Baniecki, M. Ishii, K. Kurihara, K. Yamanaka, T. Yano, K. Shinozaki, T. Imada, K. Nozaki, and N. Kin, Photoemission and quantum chemical study of $SrTiO_3$ (001) surfaces and their interaction with $CO_2$, Phys. Rev. B **78**, 195415 (2008).

[35] Z. Q. Liu, W. M. Lü, X. Wang, Z. Huang, A. Annadi, S. W. Zeng, T. Venkatesan, and Ariando, Magnetic-field induced resistivity minimum with in-plane linear magnetoresistance of the Fermi liquid in $SrTiO_{3-x}$ single crystals, Phys. Rev. B **85**, 155114 (2012).

[36] W. Gong, H. Yun, Y. B. Ning, J. E. Greedan, W. R. Datars, and C. V. Stager, Oxygen-deficient $SrTiO_{3-x}$, $x = 0.28$, 0.17, and 0.08. Crystal growth, crystal structure, magnetic, and transport properties, J. Solid State Chem. **90**, 320 (1991).

[37] X. Lin, C. W. Rischau, L. Buchauer, A. Jaoui, B. Fauqué, and K. Behnia, Metallicity without quasi-particles in room-temperature strontium titanate, npj Quantum Mater. **2**, 41 (2017).

[38] A. Spinelli, M. A. Torija, C. Liu, C. Jan, and C. Leighton, Electronic transport in doped $SrTiO_3$: Conduction mechanisms and potential applications, Phys. Rev. B **81**, 155110 (2010).

[39] O. N. Tufte and P. W. Chapman, Electron mobility in semiconducting strontium titanate, Phys. Rev. **155**, 796 (1967).

[40] P. A. Lee and T. V. Ramakrishnan, Disordered electronic systems, Rev. Mod. Phys. **57**, 287 (1985).

[41] C. Barone, H. Rotzinger, C. Mauro, D. Dorer, J. Münzberg, A. V. Ustinov, and S. Pagano, Kondo-like transport and magnetic field effect of charge carrier fluctuations in granular aluminum oxide thin films, Sci. Rep. **8**, 13892 (2018).

[42] K. S. Takahashi, D. Matthey, D. Jaccard, and J. Triscone, Transport properties of reduced $SrTiO_3$ single crystal thin films, Ann. Phys. **516**, 68 (2004).

[43] H. P. R. Frederikse, W. R. Thurber, and W. R. Hosler, Electronic transport in strontium titanate, Phys. Rev. **134**, A442 (1964).

[44] E. Sawaguchi, A. Kikuchi, and Y. Kodera, Microscopic examination of $SrTiO_3$ at low temperatures, J. Phys. Soc. **18**, 459 (1963).

[45] H. E. Weaver, Dielectric properties of single crystals of $SrTiO_3$ at low temperatures, J. Phys. Chem. Solids **11**, 274 (1959).

[46] D. Joung and S. I. Khondaker, Efros-Shklovskii Variable-range hopping in reduced graphene oxide sheets of varying carbon $Sp^2$ fraction, Phys. Rev. B **86**, 235423 (2012).

[47] N. Mott, M. Pepper, S. Pollitt, R. H. Wallis, and C. J. Adkins, The Anderson transition, Proc. R. Soc. London, Ser. A **345**, 169 (1975).

[48] A. L. Efros and B. I. Shkylovskii, Coulomb gap and low temperature conductivity of disordered systems, J. Phys. C Solid State Phys. **8**, L49 (1975).

[49] H. Trabelsi, M. Bejar, E. Dhahri, M. Sajieddine, M. A. Valente, and A. Zaoui, Effect of the oxygen deficiencies creation on the suppression of the diamagnetic behavior of $SrTiO_3$ compound, J. Alloys Compd. **680**, 560 (2016).

[50] M. Khalid, A. Setzer, M. Ziese, P. Esquinazi, D. Spemann, A. Pöppl, and E. Goering, Ubiquity of ferromagnetic signals in common diamagnetic oxide crystals, Phys. Rev. B **81**, 214414 (2010).

[51] J. N. Eckstein, Watch out for the lack of oxygen, Nat. Mater. **6**, 473 (2007).

[52] D. A. Muller, N. Nakagawa, A. Ohtomo, J. L. Grazul, and H. Y. Hwang, Atomic-scale imaging of nanoengineered oxygen vacancy profiles in $SrTiO_3$, Nature (London) **430**, 657 (2004).

[53] S. Zhang, D. Guo, M. Wang, M. S. Javed, and C. Hu, Magnetism in $SrTiO_3$ before and after UV irradiation, Appl. Surf. Sci. **335**, 115 (2015).

[54] Y. Zhang, J. Hu, E. Cao, L. Sun, and H. Qin, Vacancy induced magnetism in $SrTiO_3$, J. Magn. Magn. Mater. **324**, 1770 (2012).

[55] N. Mott, *Metal-Insulator Transitions*, 1st ed. (CRC Press, Taylor & Francis, London, 1990).

[56] W. N. Shafarman, D. W. Koon, and T. G. Castner, dc conductivity of arsenic-doped silicon near the metal-insulator transition, Phys. Rev. B **40**, 1216 (1989).

[57] T. Tanaka, K. Matsunaga, Y. Ikuhara, and T. Yamamoto, First-Principles Study on Structures and Energetics of Intrinsic Vacancies in $SrTiO_3$, Phys. Rev. B **68**, 205213 (2003).

[58] T. Mizoguchi, Y. Sato, J. P. Buban, K. Matsunaga, T. Yamamoto, and Y. Ikuhara, Sr vacancy segregation by heat treatment at $SrTiO_3$ grain boundary, Appl. Phys. Lett. **87**, 241920 (2005).

[59] T. Yamamoto, T. Mizoguchi, S. Y. Choi, Y. Sato, N. Shibata, and Y. Ikuhara, Grain Boundary Atomic Structures in $SrTiO_3$ and $BaTiO_3$, in *Materials Science Forum* (Trans Tech Publ, Stafa-Zurich, Switzerland, 2007), Vol. 558-559, pp. 851–856.

[60] M. Youssef, B. Yildiz, and K. J. Van Vliet, Thermomechanical stabilization of electron small polarons in $SrTiO_3$ assessed by the quasiharmonic approximation, Phys. Rev. B **95**, 161110(R) (2017).

[61] M. Choi, F. Oba, Y. Kumagai, and I. Tanaka, Antiferrodistortive-like oxygen-octahedron rotation induced by the oxygen vacancy in cubic $SrTiO_3$, Adv. Mater. **25**, 86 (2013).

[62] D. Kan, T. Terashima, R. Kanda, A. Masuno, K. Tanaka, S. Chu, H. Kan, A. Ishizumi, Y. Kanemitsu, Y. Shimakawa, and M. Takano, Blue-light emission at room temperature from Ar + -irradiated $SrTiO_3$, Nat. Mater. **4**, 816 (2005).

[63] M. M. Parish and P. B. Littlewood, Classical magnetotransport of inhomogeneous conductors, Phys. Rev. B **72**, 094417 (2005).

[64] Z. H. Wang, L. Yang, X. J. Li, X. T. Zhao, H. L. Wang, Z. D. Zhang, and X. P. A. Gao, Granularity controlled nonsaturating linear magnetoresistance in topological insulator $Bi_2$ $Te_3$ films, Nano Lett. **14**, 6510 (2014).

[65] A. Narayanan, M. D. Watson, S. F. Blake, N. Bruyant, L. Drigo, Y. L. Chen, D. Prabhakaran, B. Yan, C. Felser, T. Kong, P. C. Canfield, and A. I. Coldea, Linear Magnetoresistance Caused by Mobility Fluctuations in N-Doped $Cd_3As_2$, Phys. Rev. Lett. **114**, 117201 (2015).

[66] J. C. W. Song, G. Refael, and P. A. Lee, Linear magnetoresistance in metals: guiding center diffusion in a smooth random potential, Phys. Rev. B **92**, 180204(R) (2015).

[67] J. Hu and T. F. Rosenbaum, Classical and quantum routes to linear magnetoresistance, Nat. Mater. **7**, 697 (2008).

[68] M. Kim, G. Duscher, N. D. Browning, K. Sohlberg, S. T. Pantelides, and S. J. Pennycook, Nonstoichiometry and the Electrical Activity of Grain Boundaries in $SrTiO_3$, Phys. Rev. Lett. **86**, 4056 (2001).

[69] L. F. Mattheiss, Effect of the 110° K phase transition on the $SrTiO_3$ conduction bands, Phys. Rev. B **6**, 4740 (1972).

[70] W. D. Rice, P. Ambwani, M. Bombeck, J. D. Thompson, G. Haugstad, C. Leighton, and S. A. Crooker, Persistent optically induced magnetism in oxygen-deficient strontium titanate, Nat. Mater. **13**, 481 (2014).

[71] S. Hikami, A. I. Larkin, and Y. Nagaoka, Spin-orbit interaction and magnetoresistance in the two dimensional random system, Prog. Theor. Phys. **63**, 707 (1980).

[72] X. Liu, Z. Zhang, C. Cai, S. Tian, S. Kushwaha, H. Lu, T. Taniguchi, K. Watanabe, R. J. Cava, and S. Jia, Gate tunable magneto-resistance of ultra-thin W $Te_2$ devices, 2D Mater. **4**, 21018 (2017).

[73] X. Ren, Y. Wang, Z. Xie, F. Xue, C. Leighton, and C. D. Frisbie, Gate-tuned insulator–metal transition in electrolyte-gated transistors based on tellurene, Nano Lett. **19**, 4738 (2019).

[74] J. F. Schooley, W. R. Hosler, and M. L. Cohen, Superconductivity in Semiconducting $SrTiO_3$, Phys. Rev. Lett. **12**, 474 (1964).

[75] A. I. Larkin, Reluctance of two-dimensional systems, Pisma Zh. Eksp. Teor. Fiz. **31**, 239 (1980) [Sov. Phys. JETP Lett. **31**, 219 (1980)].

[76] S. Bhattacharyya, D. Mtsuko, C. Allen, and C. Coleman, Effects of Rashba-spin–orbit coupling on superconducting boron-doped nanocrystalline diamond films: Evidence of interfacial triplet superconductivity, New J. Phys. **22**, 93039 (2020).

[77] S. Lo, S. Lin, Y. Wang, and S. Lin, Spin-orbit-coupled superconductivity, Sci. Rep. **4**, 5438 (2014).

[78] S. Ohta, T. Nomura, H. Ohta, and K. Koumoto, High-temperature carrier transport and thermoelectric properties of heavily La-or Nb-Doped $SrTiO_3$ single crystals, J. Appl. Phys. **97**, 34106 (2005).